Bulletin of the Seismological Society of America, Vol. 108, No. 4, pp. 1929–1946, August 2018, doi: 10.1785/0120170314

Evidence for Tear Faulting from New Constraints of the 23 October 2011 M_w 7.1 Van, Turkey, Earthquake Based on InSAR, GPS, Coastal Uplift, and Field Observations

by Ahmet M. Akoğlu,* Sigurjón Jónsson, Teng Wang, Ziyadin Çakır, Ugur Dogan, Semih Ergintav, Batuhan Osmanoğlu, Guangcai Feng, Cengiz Zabcı, Alpay Özdemir, and Ömer Emre

Abstract The 23 October 2011 M_w 7.1 Van earthquake in eastern Turkey took place on a previously unknown thrust fault, causing over 600 fatalities and extensive damage mainly in Van city and the northern town of Erciş. Several coseismic models have already been published after the earthquake using the available seismological and geodetic data. These studies generally agree on a coseismic rupture on a north-dipping east–west-trending blind-thrust fault comprising one or two subparallel segments and the existence of a shallow slip deficit. Here, by introducing an additional coseismic pixel-offset dataset from the TerraSAR-X satellite, we conclude that a NNE–SSW-trending left-lateral tear fault that bounds the rupture to the east also slipped both during and after the mainshock, which is in agreement with both field observations and postseismic Global Positioning System (GPS) measurements. This has important implications for the seismic hazard analysis of the region as the extent and geometry of the rupture that we infer differ significantly from those previously proposed.

Electronic Supplement: Figures showing comparison of the descending-mode Envisat Interferometric Synthetic Aperture Radar (InSAR) data and fault parameter trade-offs.

Introduction

The 23 October 2011 (13:41, GMT+2) M_w 7.1 Van earthquake was the first $M_w > 7$ event to occur in Turkey after the devastating İzmit and Düzce earthquakes of 1999, and it remains the largest instrumentally recorded thrust-faulting event to strike the Turkish–Iranian plateau since the 1988 M_s 6.8 Spitak, Armenia, earthquake (Fig. 1). Although the epicentral area has a rich history of civilization, not much was known from the active tectonics perspective before the earthquake. Causing a loss of > 600 lives and extensive damage in Van and surrounding villages, the event resulted in an estimated economical loss of up to $1.5 billion U.S. (Bevere *et al.*, 2012). The official figures report 117,700 damaged housing units (Erdik *et al.*, 2012), with around 10% of the damage in the town of Erciş to the north of Lake Van (Fig. 1).

Early focal mechanism solutions (Table 1) showed that the earthquake took place on a fault-trending east-northeast–south-southwest and dipping either to the south or to the north, consistent with the distribution of aftershocks (Fig. 2). The nodal plane ambiguity could not be solved after extensive field studies as no convincing evidence of a clear surface rupture related with the main fault was found in the field. Some compressional deformation observed along a short distance crossing the Van-Erciş highway (Fig. 3) was attributed to a northward-dipping main fault rupture (Emre *et al.*, 2011). However, these might also have possibly been associated with back thrusting due to a primary rupture on a south-dipping fault resolved by various focal mechanism solutions (Fig. 1). Thus, it became evident that some key parameters of the earthquake such as the location and the dip and strike direction of the causative fault could not be constrained without using space-based geodetic techniques.

Being the largest of its kind in the instrumental era in the western part of the Turkish–Iranian plateau, the Van earthquake provides an opportunity to improve our understanding of the active tectonics and continental deformation of eastern Turkey and its vicinity, and the nature of blind faulting. The latter is particularly important since active blind faults still represent one of the missing blocks of our current interpretation of seismic hazard models (Dolan *et al.*, 2003). This

*Now at Istanbul Technical University, Department of Geology, Ayazağa Yerleşkesi, Sarıyer 34469, Istanbul, Turkey.

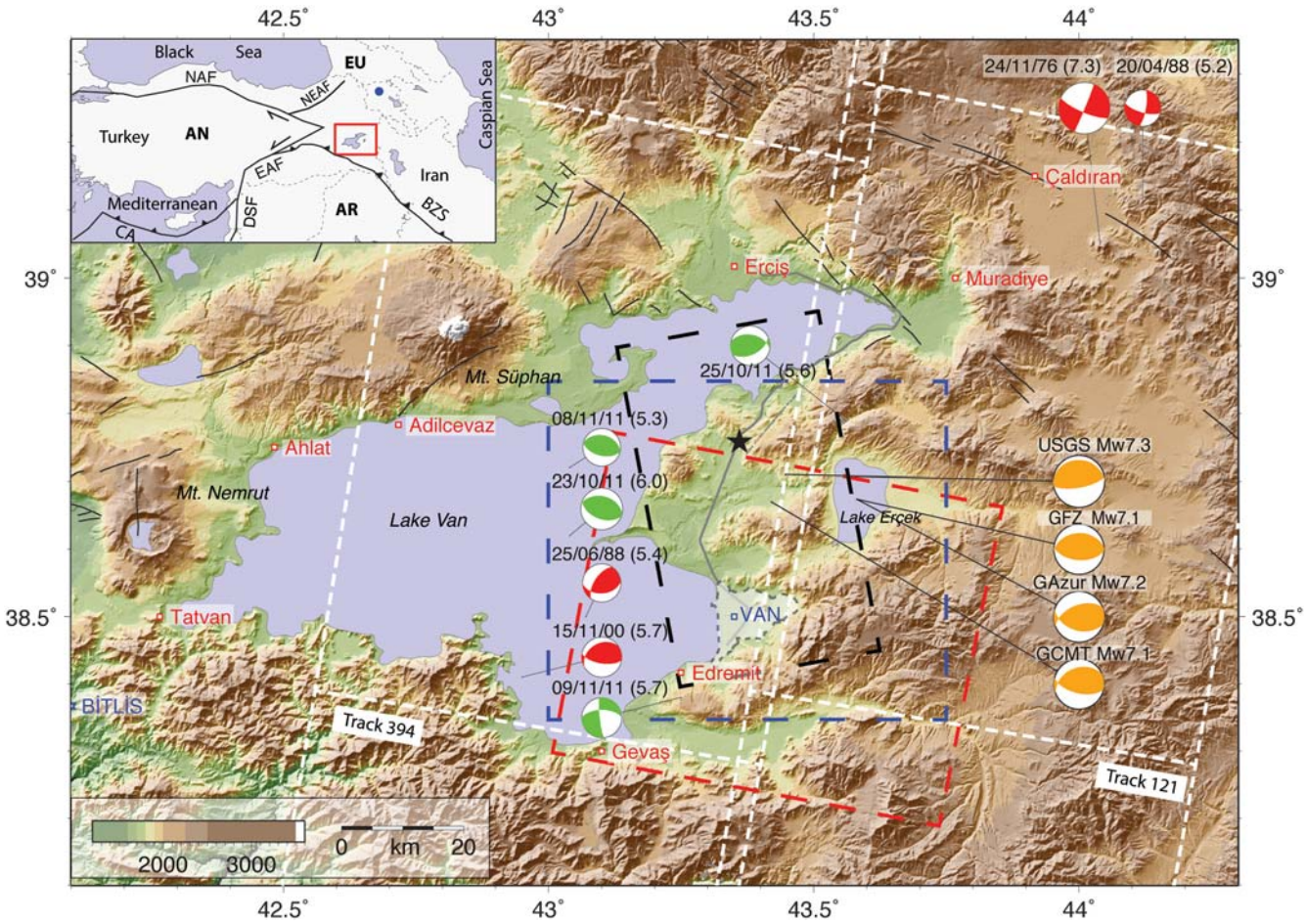

Figure 1. Map of the Van region showing known active faults (black lines from Şaroglu *et al.*, 1992), shaded topography (from Shuttle Radar Topography Mission [SRTM] 90 m data), and focal mechanisms of several earthquakes. Solutions for the 2011 Van mainshock by different research groups/institutions are shown in orange, whereas green and red ones show solutions for a few aftershocks and previous events, respectively. The black star indicates the epicenter of the Van earthquake as determined by the Kandilli Observatory. The white, red, and black rectangles represent the Synthetic Aperture Radar (SAR) scene coverage of Envisat (T394 and 121), Cosmo-SkyMed (CSK), and TerraSAR-X satellites, respectively. The blue dashed rectangle is the area shown in Figure 3. The region marked with a black dashed line around Van represents the city center where most of the population is settled. The gray line connecting Van and Erciş is the highway mentioned in the Introduction. (Inset) Study area in the context of Eurasia–Arabia convergence, where the blue dot shows the location of Spitak, Armenia (AN, Anatolian plate; AR, Arabian plate; BZS, Bitlis Zagros suture; CA, Cyprus arc; DSF, Dead Sea fault; EAF, East Anatolian fault; EU, Eurasian plate; NAF, North Anatolian fault; NEAF, Northeast Anatolian fault).

is simply because of the fact that earthquakes on concealed faults, especially with longer recurrence intervals and with a weak surface morphology, are difficult to identify. During the last three decades of the instrumental era, several prominent blind-faulting events on unknown-unstudied faults occurred around the world causing extensive damage and loss of lives, with the 2010 M_w 7.0 Haiti earthquake being the most prominent example (Calais *et al.*, 2010).

Several studies based on Interferometric Synthetic Aperture Radar (InSAR) observations of the Van earthquake have already been published (Elliott *et al.*, 2013; Fielding *et al.*, 2013; Feng *et al.*, 2014; Moro *et al.*, 2014; Wang *et al.*, 2015; Trasatti *et al.* 2016). All these studies are however limited to coseismic Synthetic Aperture Radar (SAR) datasets only from the descending orbit and far-field Global Positioning System (GPS) data, which makes it difficult to constrain both the geometry of the fault rupture(s) and the rake angle accurately, and hence the distribution of reverse- and strike-slip components on the fault surface. There is also an important difference particularly in the proposed fault geometries; while one group of researchers (Elliott *et al.*, 2013; Wang *et al.*, 2015) proposes a two-fault model, others suggest a single segment. Nonetheless, both group of studies agree on a deeply buried coseismic slip (10–22 km) on a north-dipping fault and a lack of slip at shallower depths (< 8 km). Furthermore, later studies focusing mainly on the postseismic movements after the earthquake by Dogan *et al.* (2014) and Mackenzie *et al.* (2016) brought into light the existence of another active fault to the south that cuts through the city center of Van.

In order to validate whether a two-segment fault is the appropriate model for the Van earthquake and to improve the

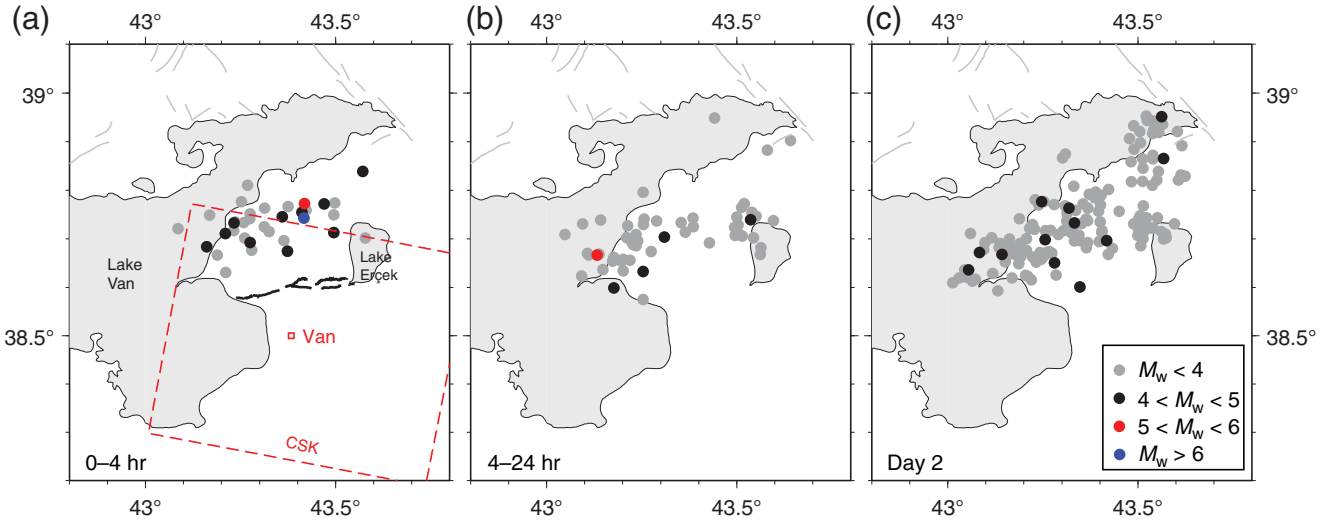

Figure 2. Aftershock activity for the first two days from the relocated catalog of Işık *et al.* (2017). Gray lines show the active faults from the former Turkish General Directorate of Mineral Research and Exploration (MTA) catalog of Şaroğlu *et al.* (1992). (a) Activity in the first 4 hr with the red rectangle representing the CSK scene coverage. (b) Activity during the rest of the day with (c) showing the activity on the second day.

uncertainties in the source parameters that inevitably result from the use of only one type of SAR imaging geometry (Sudhaus and Jónsson, 2009); here in this study, we introduce an X-band SAR pixel-offset dataset that was neglected by the previous studies due to lack of coherence owing to its long temporal baseline (Table 2). This additional new SAR dataset from the German TerraSAR-X satellite captures the surface deformation from a different angle of view (i.e., ascending orbit). Added to that we also make use of data from near-field coseismic GPS stations as well as a set of coastal uplift measurements made along the shores of Lake Van, which should further help reducing model parameter trade-offs and uncertainties.

Our article starts with a brief introduction of the seismotectonics of the region, followed by a description of the data and then we discuss the importance of adding ascending pixel offsets to our analysis. We conclude our study after making comparisons to the previously published coseismic models and discussing our inferences on the nature of the rupture.

Table 1
Source Parameters of the Mainshock from Seismology and Geodesy-Based Studies

	Strike (°)	Dip (°)	Rake (°)	M_0 (10^{19} N · m)	M_w
Seismology based					
USGS centroid moment	272	19	101	9.937	7.3
	80	71	86		
USGS body-wave moment tensor	255	50	73	6.398	7.1
	101	43	109		
USGS *W* phase	241	51	58	5.598	7.1
	106	49	123		
Global CMT catalog	246	38	60	6.27	7.1
	103	58	112		
Irmak *et al.* (2012)	246	46	59	5.53	7.13
Geodesy based					
Fielding *et al.* (2013)	259	42.5	-	5.84	7.13
Elliott *et al.* (2013) (two-fault model)	254	40	64	4.8	7.1
	254	55	93		
Moro *et al.* (2014)	252	50.3	74.4		7.12
Feng *et al.* (2014)	261.3	49	88	4.19	7.03
Wang *et al.* (2015)	253	40	Free	6.08	7.19
	253	54			
Trasatti *et al.* (2016)	263	50	72	5.5	7.1
This study (single fault)	262	54	Free	5.55	7.13
			(42.58)		
This study (two-fault model)	262	56	Free	6.1	7.16
	195	60	(34.06)		

Average rake values for our models are given inside parentheses. USGS, U.S. Geological Survey; CMT, Centroid Moment Tensor (Ekström *et al.*, 2012).

Seismotectonics

Eastern Turkey is a part of a 2-km-high plateau that results from the continental collision between the Arabian and Eurasian plates (Dewey *et al.*, 1986) that started about middle-late Miocene (Şengör *et al.*, 1985) with the closure of the Tethys Ocean. Based on theoretical studies and the direction of plate convergence later confirmed by GPS measurements (McClusky *et al.*, 2000; Reilinger *et al.*, 2006), the continental deformation was claimed by Şengör *et al.* (1985) and Dewey *et al.* (1986) to be driven by north–south compression and accommodated by postulated east–west-trending reverse faults, northwest–southeast-striking right-lateral

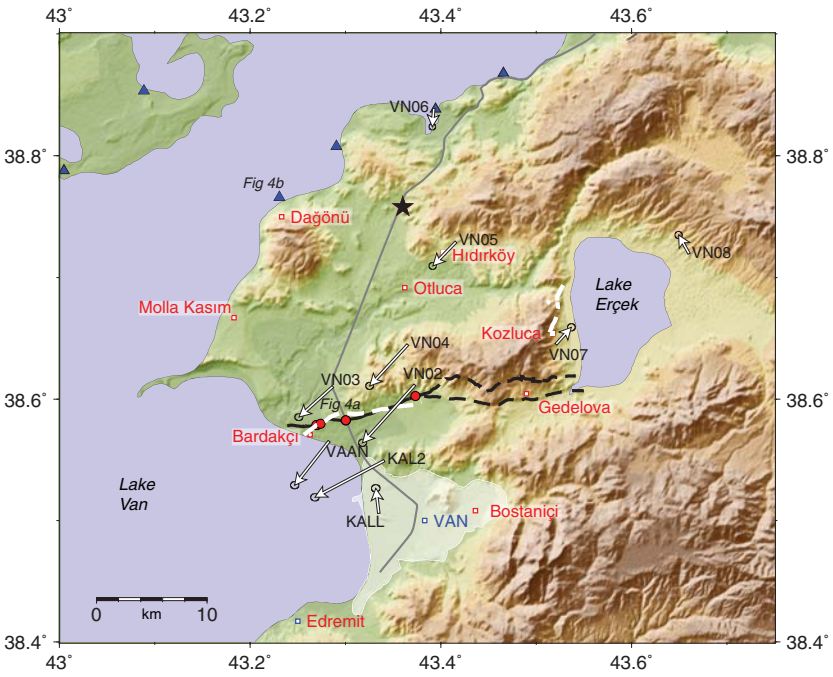

Figure 3. Map of the epicentral area (black star shows the epicenter) marked with a blue dashed rectangle in Figure 1. Blue triangles represent part of the sites where coastal uplift was measured. The gray line is the Van–Erciş highway. The red dots are the locations where deformation on man-made structures was observed during the reconnaissance studies of Akyüz *et al.* (2011). The continuous part of the black line drawn between Lake Van and Erçek represents the zone where compressional structures were observed on the surface after the earthquake. The eastern dashed half of the same line represents the verdict of MTA researchers (Emre *et al.*, 2011) as the continuation of the fault on the surface after an analysis of the surface morphology (via air photos, etc.). White dashed lines represent surface discontinuities reported by Doğan and Karakaş (2013). White arrows show the postseismic Global Positioning System (GPS) movement as reported by Dogan *et al.* (2014).

strike-slip faults (e.g., North Anatolian and Çaldıran-Tabriz faults) and northeast–southwest-trending left-lateral strike-slip faults (e.g., East Anatolian Fault). The GPS velocity field of Reilinger *et al.* (2006) indicates that up to 10 mm/yr of the convergence between the Arabian and Eurasian plates varies rather smoothly within a wide region from the Bitlis Suture to the south to the Northeast Anatolian Fault to the north (Mackenzie *et al.*, 2016; Fig. 1). This suggests a relatively low rate of strain accumulation on individual thrust faults which are distributed within this large region, which in turn implies long recurrence intervals for large earthquakes on them. This might explain the absence of thrust faults of any orientation in published active fault maps of the region, including the (now outdated) one of Turkish General Directorate of Mineral Research and Exploration (MTA, Şaroğlu *et al.*, 1992), likely due to removal of surface expression of active faulting during long interseismic periods, and the absence of major thrust-faulting events before the 2011 Van earthquake. Thrust-faulting earthquakes in the region prior to the Van event were few, scattered, and small and, thus, claimed (Örgülü *et al.*, 2003) to be the manifestation of their minor contribution to the ongoing plate convergence in an escape tectonics regime. The Van earthquake with its moment magnitude over 7 therefore, to some extent, was a surprise and, thus, has provided an opportunity to refine the models of active continental deformation in the Turkish Iranian Plateau as explained earlier.

The first major earthquake to occur in the instrumental period off the North and East Anatolian Fault, before the 2011 Van event, was the 1976 M_w 7.1 Çaldıran event that took place on the Çaldıran segment of the right-lateral West Azerbaijan–Turkey Shear Zone that runs about 500 km in the northwest–southeast direction between Çaldıran in Turkey and Tabriz in Iran (Karimzadeh *et al.*, 2013; Berberian, 2014). The event produced a surface rupture of about 50 km (Toksöz *et al.*, 1977; Selçuk *et al.*, 2016).

Table 2
Dataset Used in This Study and Related Misfits

Dataset	Track	Dates (yyyy/mm/dd)	Bp (m)	dT (days)	Postseismic Period Captured	Incidence Angle (°)	Wavelength (cm)	Orbit	Data Points	Weight (%)	rms Single Fault (m)	rms Two Faults (m)
CSK	—	2011/10/10 2011/10/23	193	13	4 hr	29	X(3.1)	Descending	678	74	0.0629	0.0341
ENV	394	2011/07/22 2011/11/19	221	120	27 days	41	C(5.6)	Descending	53	3	0.0207	0.0232
ENV	121	2010/11/05 2011/10/31	138	360	8 days	41	C(5.6)	Descending	365	16	0.0427	0.0501
TSX	69	2009/03/29 2011/10/31	−40	946	8 days	33.2	X(3.1)	Ascending	354	5	0.1453	0.1533
GPS	—	—	—	—	7 days	—	—	—	10	1.7	0.1054	0.0765
Coastal uplifts	—	—	—	—	2 days	—	—	—	9	0.3	0.0945	0.0941

Bp, perpendicular baseline; dT, temporal baseline; rms, root mean square; CSK, Cosmo-SkyMed; ENV, Envisat; TSX, TerraSAR-X; GPS, Global Positioning System.

The thickness of the seismogenic layer beneath this part of eastern Anatolia is estimated to reach up to a depth of 20 km on the basis of seismological activity (Örgülü *et al.*, 2003; Tan, 2004; Pınar *et al.*, 2007). After the Cornell-Kandilli Eastern Turkey Seismic Experiment (ETSE) project in the last decade (Türkelli *et al.*, 2003), the region was also revealed to have the thinnest crust in the Eastern Anatolian Plateau (Zor *et al.*, 2003).

Field Observations

Although different tectonic studies have been conducted in the region (Ketin, 1977; Aksoy and Tatar, 1990; Koçyiğit *et al.*, 2001; Özkaymak, 2003; Dhont and Chorowicz, 2006), existence of an east-northeast–west-southwest-trending thrust fault revealed by focal mechanism solutions of the 2011 Van earthquake that is capable of an $M_w > 7$ earthquake was not previously reported. Following the earthquake, field studies conducted by various groups did not reveal a clear prominent surface rupture either (Akyüz *et al.*, 2011; Emre *et al.*, 2011; Doğan and Karakaş, 2013). However, some compressional features with throws of up to 10-cm high were observed on man-made structures (Fig. 3, red circles around Bardakçı) that are aligned along a 4-km-long east–west-oriented zone, ~13 km north of the Van city center. A clear example of this compressional deformation over a concrete irrigation channel is shown in Figure 4a where up to 7 cm of throw was observed. These compressional structures located to the south of the earthquake epicenter were interpreted as the surface trace of a north-dipping thrust fault that ruptured at depth during the earthquake. However, they might as well have been formed as a result of back thrusting associated with slip on a south-dipping main fault. Thus, field observations alone failed to provide a confident solution to the nodal plane ambiguity in focal mechanisms.

In addition to the brittle surface deformation related to movement on the main fault, secondary deformational structures were also observed. As documented in detail by Akyüz *et al.* (2011), several instances of lateral spreading, subsidence, liquefaction, slump, and landslides are observed that were related to shaking and soil behavior.

An additional zone of deformation that was neglected by previous studies was the one reported by Doğan and Karakaş (2013) just to the west of Lake Erçek (Fig. 3, white dashed line). Named by the authors as the Kozluca fault, the main features observed are tensional ground cracks interpreted as evidence of left-lateral motion. The zone extends for ~4 km on the surface with a strike of ~N5°–N20°E.

Dataset Used

Coastal Uplift Measurements

Earthquakes causing coastal uplifts often form white bands of dead algae as a result of desiccation and their exposure to sun light along rocky coastlines, providing a distinctive marker suitable for quantifying the uplift (Ortlieb *et al.*, 1996; Meghraoui *et al.*, 2004; Hayes *et al.*, 2010). Similarly, observations along the coast of Lake Van between Van and Erciş also revealed similar scenes marking the clear shoreline retreat as a result of lake floor uplift. These white band levels were measured by an MTA team two days after the earthquake (Emre *et al.*, 2011) at nine different locations by measuring the vertical height difference from the lake water surface to the middle of the white-colored band of dead algae on the rock surfaces (Fig. 4b). However, the exact type of algae at these observation sites was not studied in detail following the earthquake, increasing the uncertainty in the determination of the mean water level before the earthquake. Therefore, these measurements should be taken as maximums. The lake water level reaches its minimum in September after a seasonal drop of ~25 cm. The tidal height variation of the lake surface is negligible. The maximum values measured by the MTA team reach up to 40 cm near the village of Dağönü and decrease toward the Erciş coast, as expected from a reverse faulting on a northward-dipping fault (Fig. 5).

Coseismic GPS Measurements

Although continuous and campaign-type GPS benchmarks were present in the area before the Van earthquake, only a few of them were located within a distance of 50 km from the epicenter (Fig. 5). Ten benchmarks of the Turkish National Fundamental GPS Network (TFGN-99A) were reoccupied once for 8–10 hr about six days after the earthquake. Pre-earthquake GPS surveys were carried out two years before the event and the velocity field of Reilinger *et al.* (2006) was used to remove the secular motion. The GPS data processing is similar to Dogan *et al.* (2014). The network was adjusted by fixing the International Terrestrial Reference Frame (ITRF) 2008.0, epoch 2011 coordinates of the ZECK station in Caucasia (Russia) from the Scripps Orbit and Permanent Array Center, and coseismic displacements are calculated with respect to the same International GNSS Service station.

As shown in Figure 5 with 95% confidence ellipses, while the GPS vectors around the city show northward and downward displacements, those in the north show southward and upward coseismic motion. The largest horizontal displacements reaching $\sim 30 \pm 0.18$ cm were observed north of the city's metropolitan area (i.e., at KAL2). Maximum subsidence of $\sim 30 \pm 0.55$ cm was observed at the VAAN station very close to the aforementioned compressional features seen on man-made structures. The subsidence and large northward displacement observed on this particular station demonstrate that it should be located on the footwall block of the fault and, thus, helps us constrain the location of our model fault as it is not possible to pinpoint the exact location from InSAR data alone due to the lack of surface ruptures. This is consistent with the inference that surface deformations observed in the field north of Van city delineate the up-dip trace of the causative coseismic fault.

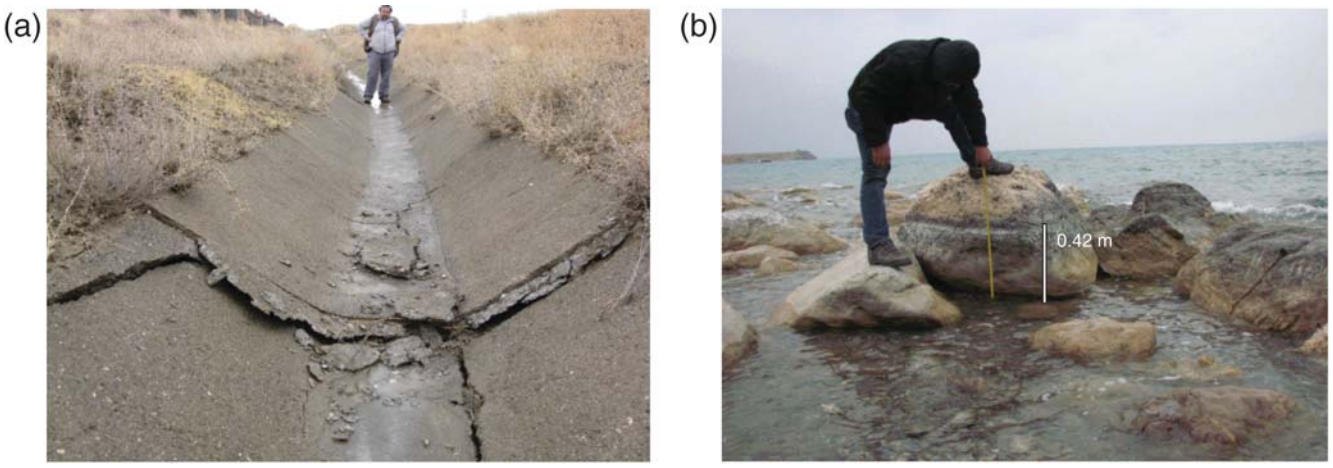

Figure 4. (a) Photo showing an example of the surface deformation observed on man-made structures where around 7 cm of vertical displacement was measured on an irrigation channel (Location 2 at Akyüz *et al.*, 2011, coordinates: 43.269319°, 38.578798°). Photo is toward the south. (b) Coastal uplift of ~40 cm on the coast near Dağönü village measured two days after the event (photo from Emre *et al.*, 2011).

InSAR Dataset

The first available coseismic InSAR dataset came from the Cosmo-SkyMed (CSK) satellite of Italian Space Agency (Table 2 and Fig. 6a). We processed the interferogram using GAMMA software (Werner *et al.*, 2000). The postevent image was acquired only 4 hr after the earthquake, so these InSAR data can be assumed to contain limited postseismic deformation. The overall coherence of the interferogram is fairly high due to a short temporal baseline of only 12 days and sparsely vegetated surface cover of the area. However, some coherence is lost on steep slopes and at high elevations, probably due to the imaging geometry and change in snow cover. Signal decorrelation also occurs along the zones of compressional surface deformation to the west due to a high fringe rate.

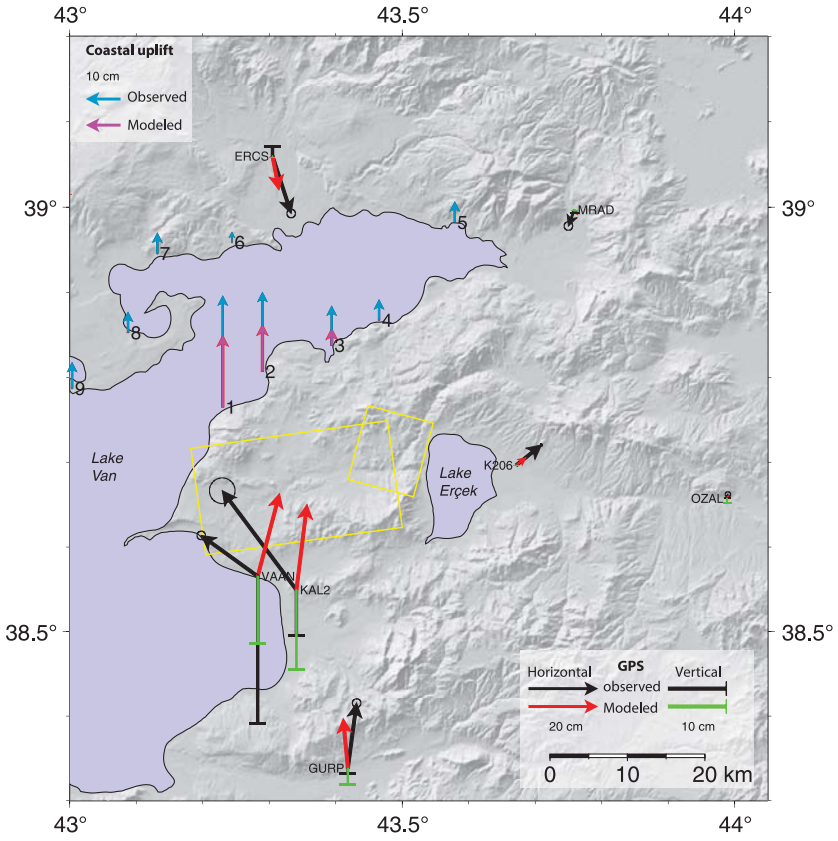

Figure 5. Coastal uplifts (Emre *et al.*, 2011), coseismic GPS measurements and their related model predictions are shown with light blue, black, magenta and red (green for the vertical component) arrows, respectively. The model predictions are for the two-fault model shown in Figure 11. Yellow rectangles represent the surface projection of our proposed Van and Kozluca faults.

The main feature of the earthquake that can readily be seen in the CSK interferogram (Fig. 6b) is a large deformation ellipse centered between Hıdırköy and Otluca villages ~20 km north of the Van city center, which reveals the typical doming effect of blind faulting that is not fully apparent in present-day topography, likely due to erosional processes and activation of neighboring parallel faults. The full extent of the ellipse could not be captured due to a lack of pre-earthquake images to the north. Nevertheless, its northeast–southwest-trending long axis is clearly visible and consistent with the strike of the fault planes estimated from seismology. However, this large ellipse alone does not provide strong evidence for a north-dipping fault because profiles perpendicular to the long axis of the dome and, hence, to the strike of the fault (Fig. 7a) do not display a clear asymmetry (such as vergence in fault-related folds) that shows the direction

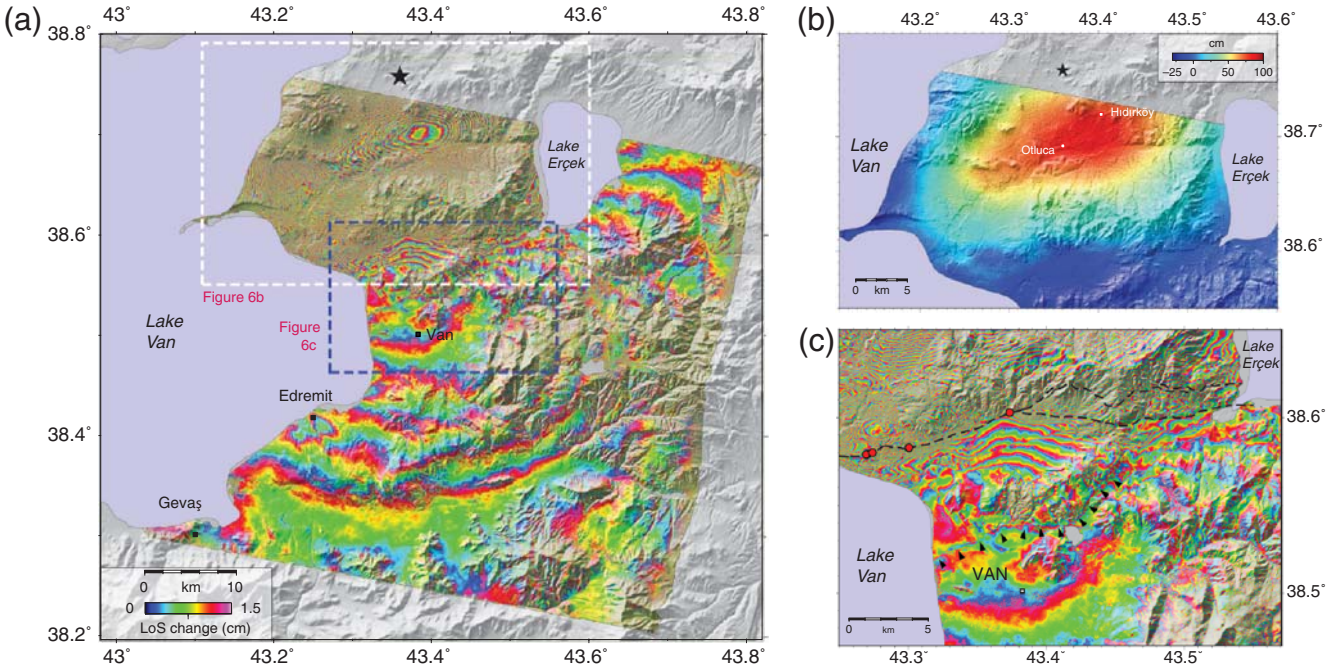

Figure 6. (a) Cosmo-SkyMed interferogram of 11–23 October 2011. Each fringe represents 1.5 cm of displacement toward the satellite. The black star shows the earthquake epicenter. (b) Enlarged view of the epicentral region showing the unwrapped line of sight (LOS) change, with positive values indicating movement of the ground up toward the satellite. (c) Enlarged view of the larger Van area. Black triangles represent the fringe discontinuities mentioned in the Discussion section.

in which thrusting takes place (King and Vita-Finzi, 1981; Philip and Meghraoui, 1983). Supporting evidence for the north-dipping fault comes from the presence of a second lobe to the south with a similar size but with much smaller amplitude (~13 cm). The opposite sign of this displacement represents an increase in radar line of sight (LOS) meaning subsidence and/or westward movement centered in the Van metropolitan area to the south. Thus, LOS displacement profiles crossing the two lobes display an asymmetry between a larger hanging-wall uplift in the north and smaller footwall subsidence to the south, typical of a steeply dipping thrust fault (Parsons *et al.*, 2006). Counting the fringes in the main lobe in the north (~60) and assuming a pure reverse faulting for simplicity indicate an uplift with a LOS change of up to a meter. The amount of uplift, however, has to be somewhat larger if one takes into account the descending viewing geometry and the seismologically determined left-lateral slip component on the north-dipping earthquake rupture. This is because while a reverse-slip component gives rise to LOS range decrease (i.e., uplift) at the hanging wall, a left-lateral slip component results in a westerly motion, that is, a range increase (i.e., away from the satellite) reducing the overall LOS range decrease.

Another significant visual feature of the CSK interferogram is the transition between the hanging-wall and footwall blocks that is marked clearly with a distinct change in the fringe rate from north to south and a 4–5-km-long right step. Such a bend or step would not be expected from a single-segment thrust fault.

Apart from the two large lobes, there are various linear phase discontinuities visible in the interferogram, such as the ones shown in Figure 6c just north of the Van city center. These discontinuities are the manifestations of triggered small-scale slip on faults above the thrust front, a phenomenon commonly associated with large earthquakes (Wright *et al.*, 2001). Postseismic SAR imagery and GPS measurements show that some of these discontinuities continue to slip aseismically after the earthquake (Dogan *et al.*, 2014; Mackenzie *et al.*, 2016).

A second set of coseismic InSAR data comes from two tracks of the European Space Agency's C-band Envisat satellite (T121 and T394), which was operating in a drifting orbit mode during the time of the earthquake (Miranda *et al.*, 2010). The Envisat interferograms, calculated using Jet Propulsion Laboratory (JPL)/Caltech ROI_pac software (Rosen *et al.*, 2004), provide a complete overview of the deformation field thanks to their spatial coverage (Fig. 8). The overall pattern of deformation is the same as observed in the CSK interferogram. However, the data present some disadvantages for modeling. The eastern track (T121), although coherent, provides only partial information about the deformation pattern to the east of Lake Erçek as it only covers part of the epicentral region. Nevertheless, the interferogram on T121 has two partial lobes of fringes for the uplifting (~23 fringes) and subsiding (~4 fringes) blocks, respectively.

Although the interferogram on track 394 covers most of the main deformation lobe in the epicentral region, it has low coherence, making it difficult to interpret and unwrap. The earliest postearthquake Envisat scene on track 394 covering

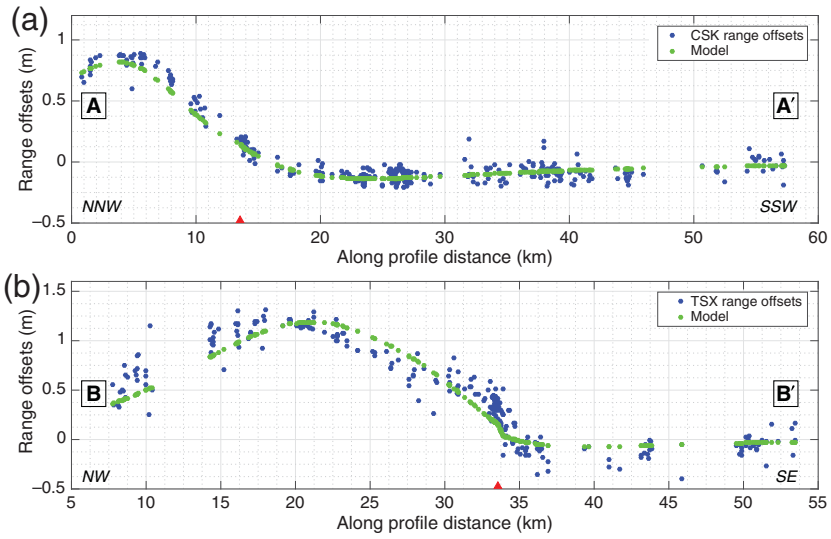

Figure 7. Comparison of the predicted LOS changes along profiles of the two-segment model (Fig. 11a) with (a) the CSK range offsets and (b) TerraSAR-X (TSX) range offsets, which were calculated at identified stable point-like scatterers. Profiles A–A′ and B–B′ are shown in Figure 9. Red triangles show the surface up-dip projection of the main fault. NNW, north-northwest; SSW, south-southwest; NW, northwest; SE, southeast.

the missing data points north of the CSK interferogram was acquired about a month after the event (Table 2). Therefore, the interferogram on this track contains a significant amount of postseismic deformation, as confirmed by the analysis of postseismic SAR and GPS data (Dogan *et al.*, 2014). The temporal difference, the drift mode of the satellite, and also the snow that started to fall in the region a couple of days after the earthquake clearly add up as a significant loss of coherence in these data, impeding the unwrapping of unconnected patches of phase values for the hanging-wall block without removing a preliminary model (Fig. 8b). In addition, the interferogram from T394 contains a set of concentric fringes due to the aftershock of 9 November 2011 (M_w 5.7) in Van city (Fig. 8c) that are also clearly evident in a separate descending postseismic TerraSAR-X interferogram (Fig. 8d). Therefore, we were limited to using only the northern (around Erciş) portion of the data from track 394 for modeling.

As a result of the problems with the Envisat data and the fact that the CSK data do not contain the entire coseismic pattern, we attempted to use an additional coseismic dataset from the German X-band TerraSAR-X (TSX) satellite (Table 2). It is worth noting that this dataset is from an ascending orbit of the satellite. The postevent scene is from eight days after the earthquake and, thus, should contain less postseismic deformation than the Envisat data. However, the large temporal baseline of 946 days between the pre- and post-earthquake scenes prevents the generation of a coherent interferogram due to strong temporal decorrelation. To overcome this problem, we make use of the technique described in Wang and Jónsson (2015) and measure coseismic offsets of stable predetected point-like scatterers, unlike the classical pixel-offset measurements calculated by cross-correlation of overlapping pixel windows. The precision and accuracy of this new dataset are significantly better than those from classical pixel offset measurements (Wang and Jónsson, 2015). High-resolution SAR sensors, such as Cosmo-SkyMed and TerraSAR-X, also provide useful pixel-offset measurements in the range direction as a possible, but often disregarded, substitute to unwrapped phase measurements. Although they contain the same LOS information as the phase values and are far less prone to possible coherence losses, range pixel offsets are generally not preferred due to their lower accuracy (~one-tenth of the pixel size).

Measuring offsets of these stable point-like scatterers therefore enabled us to use the otherwise discarded coseismic deformation information captured by the available ascending TSX pair. The maximum amount of LOS change recorded in the range direction reaches 1.4 m, around 50% higher than the range offsets of the CSK satellite, which indicates the possibility of a left-lateral movement on the fault that would contribute to the LOS decrease toward the satellite in an ascending flight configuration (Fig. 7). For the same reason, the TSX maximum lobe is shifted to the west compared with the CSK maximum values. Another important point to note is that the pixels with positive LOS change values can be observed until the Van city center to the south.

We also applied the new offset calculation technique for the CSK imagery and derived both range and azimuth offsets for this dataset (Fig. 9). Because the signal over the subsiding block from the unwrapped phase data is much clearer than the calculated range offsets, we did not opt to use the latter in modeling. On the other hand, the range offsets were crucial in the process of verifying the unwrapped values of the phase data.

As seen in Figure 9, the azimuth offsets are much noisier than the range offsets, probably due to the fact that surface displacements in the azimuth direction (east-northeast) are much smaller than those in the range (overwhelmingly vertical) direction. We therefore used the azimuth offsets only for visual comparison.

Modeling

After simplifying the earth as a homogeneous and elastic half-space, we can use the analytical solutions of Okada (1985) to relate our geodetic and coastal measurements with dislocations along rectangular planes buried in this space. To do so, we assume constant material properties (Poisson's

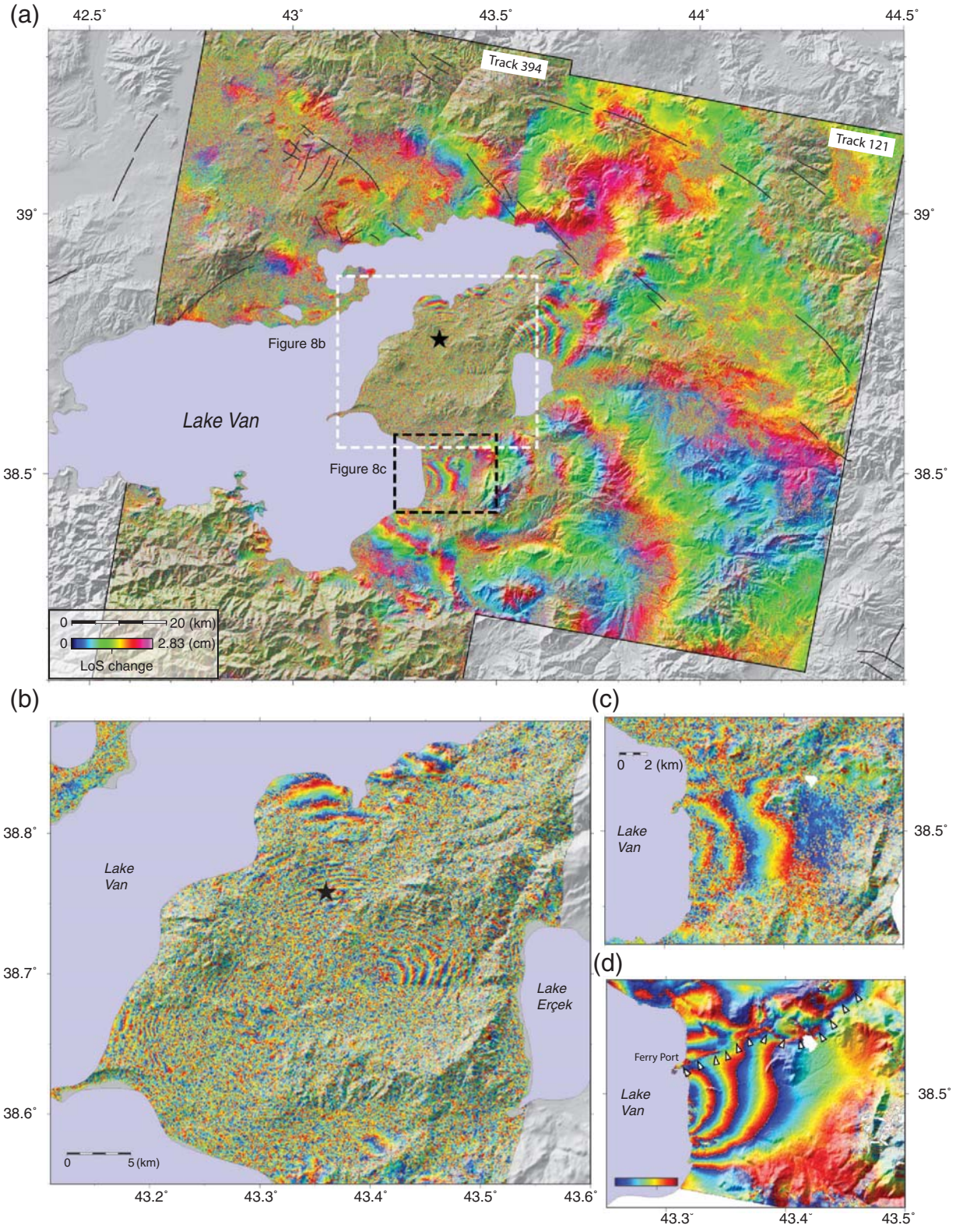

Figure 8. (a) Mosaic of Envisat descending interferograms from tracks 121 and 394 that provide complete coverage of the coseismic deformation field. Here, every fringe represents 2.83 cm of displacement toward the satellite. (b) Enlarged view of the epicentral area of track 394. Coseismic fringes are mostly disconnected due to clear loss of coherence. (c) Enlarged view of the Envisat track 394 interferogram showing concentric fringes of the 9 November aftershock in Van city. (d) Surface deformation of the same aftershock captured by TerraSAR-X descending interferogram (9–20 November 2011). Note the disturbance of the fringes along a northeast–southwest-trending zone (indicated by white triangles) passing through the Van railway ferry port, which results from the reactivation of aseismic slip on a secondary fault.

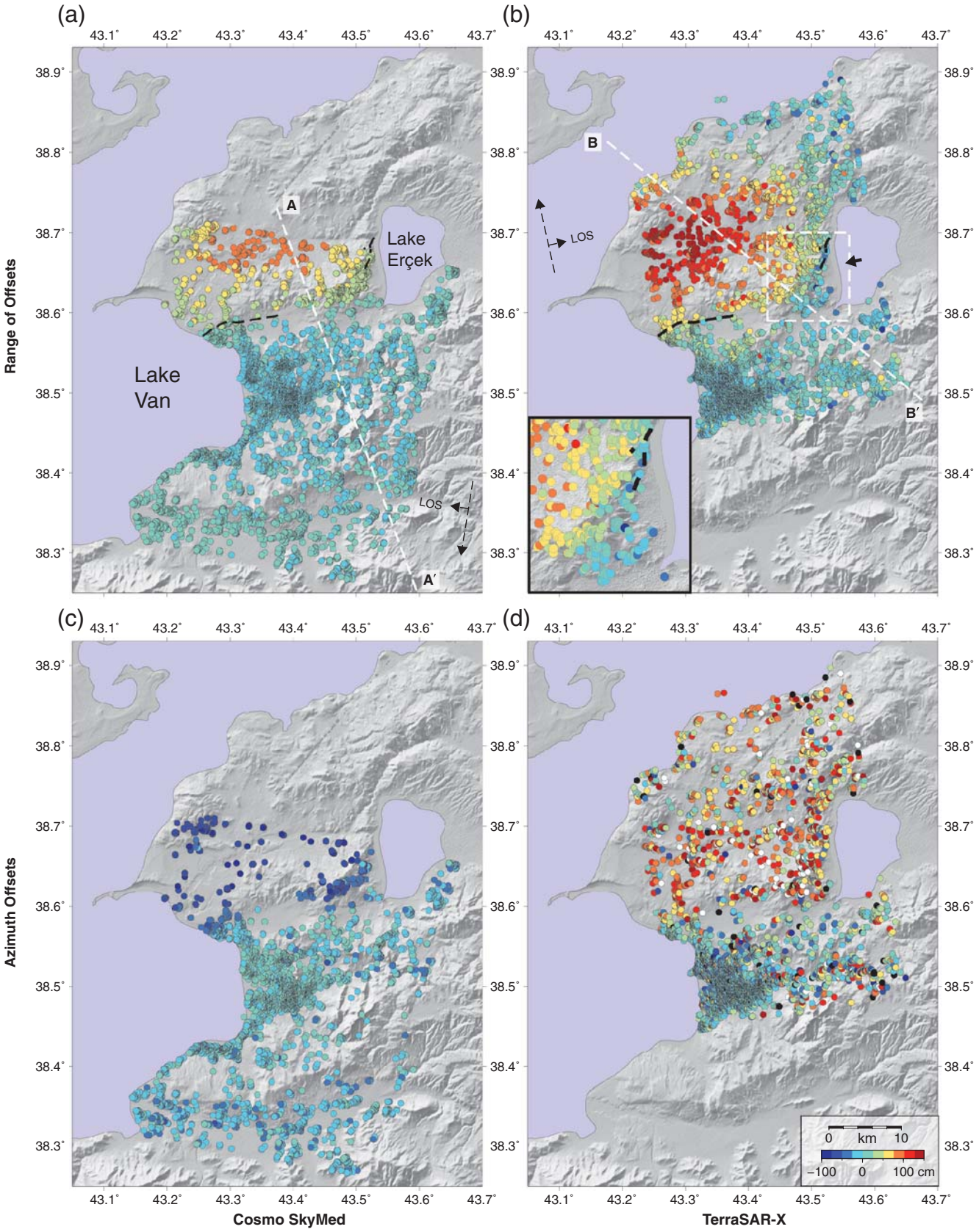

Figure 9. (a,b) Range and (c,d) azimuth pixel offsets from X-band, high-resolution SAR scenery of CSK and TerraSAR-X satellites, calculated on stable point-like scatterers. The two offshore points to the north (in b,d) are on the Adır Island. White dashed lines represent the profiles shown in Figure 7. Black dashed lines represent surface discontinuities reported by Doğan and Karakaş (2013). The dashed rectangle in (b) is the area shown in the inset.

ratio of 0.25 and a rigidity modulus of 30 GPa) and model the geodetic measurements in two steps. In the first stage, a nonlinear inversion is used to constrain the fault geometry assuming uniform slip on a single rectangular fault. In the next step, the fault found is enlarged in both the strike and the dip directions and discretized into smaller rectangular fault patches. Then, keeping the fault geometry fixed, a distributed slip model with a varying rake is found through a linear joint inversion of the InSAR (pixel offsets and unwrapped LOS displacements), GPS, and the coastal uplift measurements.

We use the fast nonnegative least squares algorithm of Bro and de Jong (1997) to invert distributed slip on the fault patches. For dip-slip dominant earthquakes, such as the Van event, the nonnegativity could become a limiting factor since the rake is allowed to vary within only 90°. To test this issue, we also followed the routine of Sudhaus and Jónsson (2009) and rotated the local in-plane coordinate axes to allow for rake variations for which both right- and left-lateral slip are allowed on patches this time between rakes of 45° and 135°. While the rakes in the shallower parts of the fault stay within 0°–90° range, the deeper parts of the fault tend to show right-lateral movements. As our geodetic datasets cannot reliably resolve these deeper parts and the fit does not improve, we can assume that a nonnegativity constraint does not bias our modeling results.

As previously discussed, we excluded the central and southern parts of the interferogram from Envisat's track 394 in the modeling due to the low coherence (hence, unwrapping errors) and the surface deformation of the 9 November 2011 M_w 5.7 aftershock. The interferogram from track 121 provides essential constraints on the termination of the rupture to the east and the depth of the coseismic slip. To reduce the number of data points in modeling, the unwrapped interferograms were subsampled using the quadtree algorithm (Jónsson *et al.*, 2002). The TSX range offset measurements are uniformly downsampled. Even though the pixel-offset dataset does not require unwrapping, there is a need to solve for its ambiguity, which was included as a term in the objective function during the inversion.

We restrict ourselves to using data from GPS sites that are inside a 160-km radius from the epicenter. In addition, because of the limited accuracy, vertical components of GPS displacements are assigned lower weights.

To estimate the uncertainties in our model parameters and the weight of each dataset, we use a Monte Carlo-based analysis in which we perturb the SAR datasets using random synthetic correlated noise. First, we infer the noise characteristics of the datasets by calculating covariograms using data samples from far-field and nondeforming regions where possible. In the case of CSK and TSX datasets, a preliminary deformation model is subtracted from the data. The 1D covariance models, which are fitted to the sample covariograms, are used to generate 100 perturbed datasets that are then inverted to get an understanding of the uncertainties of the model parameters (Sudhaus and Jónsson, 2009, 2011). It is worth noting that these uncertainties do not account for errors due to our assumptions in modeling and processing.

Modeling Results

We started the modeling process with a single fault of uniform dip and slip. Initially, the parameters were all set free. If only the CSK data are used, the strike and dip of the model fault are resolved as 70° and 54°, respectively. When data from the eastern Envisat frame (T121) are included with an equal weight, we find that the strike of the best-fitting fault increases to 76°, while its surface trace still matches the field observations northwest of Van, near Bardakçı. Addition of the TSX range data results in a southward shift of the model fault, probably due to the effect of the rapid postseismic movement in the first eight days after the earthquake.

Therefore, we decided to fix the surface trace of the fault to match a line that follows the almost east–west-trending surface observations near Bardakçı using a fixed strike of N82°E (east–west-oriented black and white lines in Fig. 3). In addition, the weights of the Envisat and TSX datasets were lowered to reduce the influence of postseismic effects.

This new round of modeling also suggests that a single $<$ 35-km-long blind-thrust-faulting event, where majority of slip occurs between 10- and 20-km depths with a maximum slip value of 10 m occurring at a depth of 16 km, can adequately explain the majority of the deformation observed on the surface (Fig. 10). The slip on the fault decreases drastically to around 1 m at shallower depths in accordance with the lack of a clear surface rupture. The model has a seismic moment of 5.55×10^{19} N · m, which corresponds to a moment magnitude of 7.13, consistent with seismologically estimated values (Table 1). Average overall root mean square values are given in Table 2.

The overall slip distribution pattern resembles previous studies despite the addition of the TSX SAR dataset from the opposite orbital viewpoint. We find a main lobe of reverse slip with an additional lobe to the west with a left-lateral strike-slip mechanism, in line with earlier studies (Fig. 10a).

Even though a simple single-segment fault model with its parameters close to seismological solutions can adequately explain most of the deformation on the surface, it raises some concerns: (1) the predicted fringe pattern on the subsiding footwall block does not match the CSK interferogram, for example, the predicted maximum subsidence occurs east of the one in the CSK interferogram (Fig. 10b), (2) the step-like transition between the hanging-wall and footwall blocks in the CSK interferogram is left unexplained, and (3) as can be seen in Figure 9b [inset] and 10c (denoted with black arrows), the TSX range offsets south of Kozluca suggest a change in the character of the deformation with a clear transition of the pixel values from positive to negative. Although the TSX data include eight days of postseismic motion after the earthquake, the existence of this discontinuity clearly hints that the main fault should not extend through

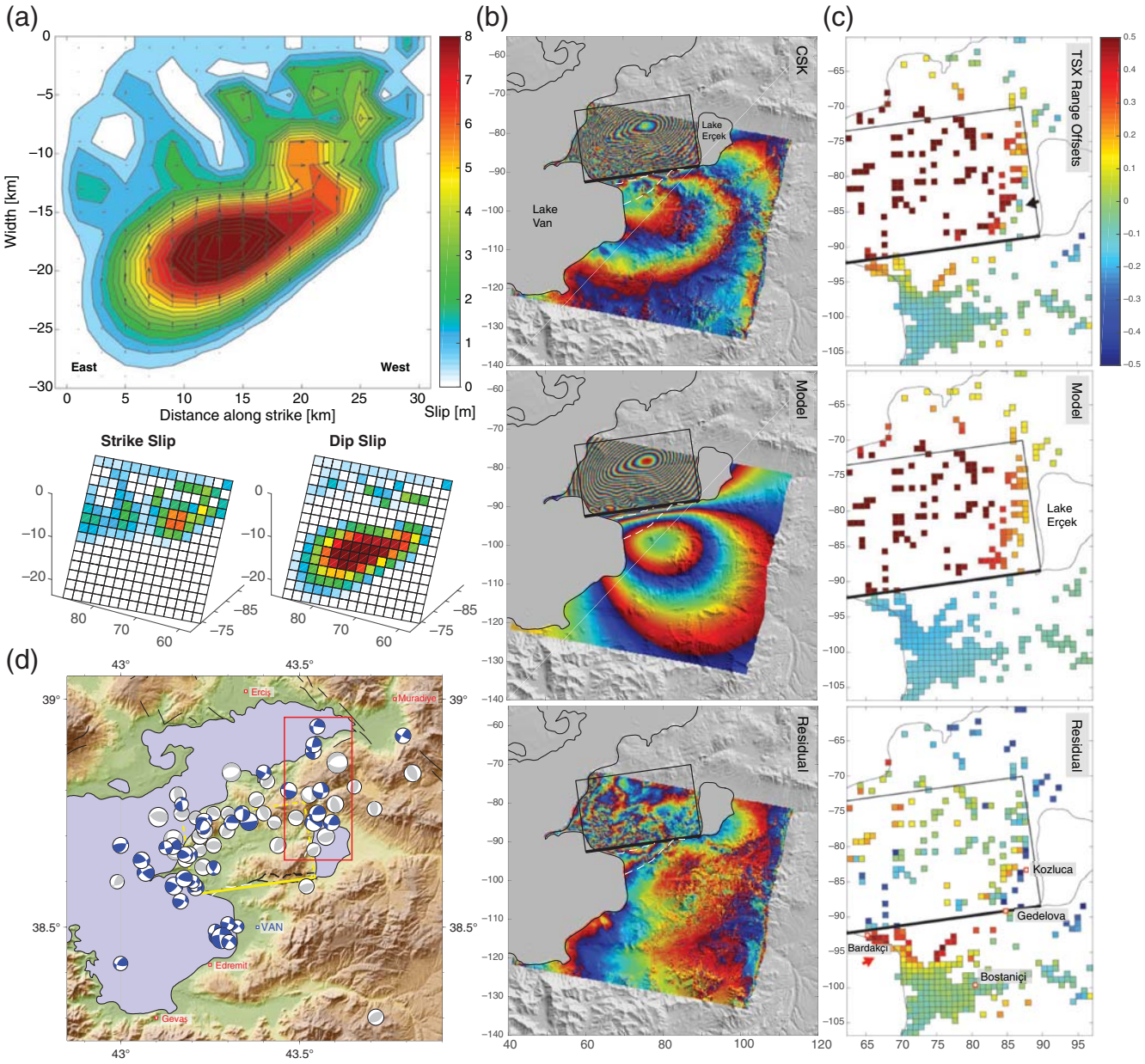

Figure 10. Modeling results for the single-segment model. (a) Slip distribution on the fault. (b) Data-model comparison of CSK-Interferometric Synthetic Aperture Radar (InSAR) data (rewrapped to 5 cm). (c) Data-model comparison of TSX SAR pixel offsets. (d) Focal mechanism solutions of aftershocks from the study of Işık *et al.* (2017). Blue and gray focal mechanism plots represent the strike-slip and dip-slip events, respectively. The red rectangle shows the border of the Cluster II of Işık *et al.* (2017). The yellow rectangle is the surface projection of our single-segment model fault.

this region further to the east. A recent study of the aftershocks by Işık *et al.* (2017) identifies a clear cluster that extends in the north–south direction, indicating the presence of left-lateral strike-slip activity in the very same region; this implies the existence of a different kind of faulting (Figs. 2c and 10d). A separate geodetic clue comes from the postseismic GPS study of Dogan *et al.* (2014), in which a station on the west coast of Lake Erçek (station VN07, Fig. 3) supports the change in character of the motion seen in the TSX range offsets. A final clue comes from the aforementioned field observations of Doğan and Karakaş (2013) around Kozluca village to the west of Lake Erçek, where surface fracturing was claimed to be associated with a coseismic left-lateral fault.

To be able to explain these features, we opt to increase the complexity of the model by introducing a second fault that follows the fracture zone mapped by Doğan and Karakaş (2013). We fixed the location and strike (N15°E) of the new segment using the information reported by the aforementioned paper and used a fixed length of 5 km for the fault in the nonlinear step of the modeling. Except for its strike (fixed to N82°E), the parameters of the main fault are set free again.

The final slip distribution due to this model is presented in Figure 11a. While the overall slip distribution along the main fault resembles the one in the single-fault scenario, the second fault shows mostly left-lateral strike-slip motion as expected from a tear fault in a thrust-faulting environment. This agrees well with the focal mechanism solutions reported by Işık *et al.* (2017). However, the errors estimated from the Monte Carlo analysis show that our dataset cannot reliably resolve some of the parameters of this segment (Ⓔ Fig. S3, available in the electronic supplement to this article). This is mainly because there are almost no data on the eastern side of the tear fault due to the presence of Lake Erçek. In addition to a fixed length, a dip of 60°, which is somewhat gentler than expected for a tear fault, is kept fixed as it better explains the fringe pattern in the footwall block.

Discussion

The addition of a secondary fault clearly helps explain the features outlined in the previous section, in addition to improving the overall fit to the data (Table 2). The left-lateral movement along the secondary fault shifts the maximum subsidence toward Lake Van, as observed in the CSK interferogram, and the overall fringe pattern follows the original data quite well. The easternmost extent of the main fault is now consistent with the TSX range-offset data, which show a clear discontinuity to the south of our second fault (toward Gedelova) that we interpret as range change occurring in the first eight days following the earthquake (denoted with a black arrow in both Figs. 9b [inset] and 10c). Because of the improvement in the fit to the CSK data by the addition of this segment, we think that the surface tensional cracks that were reported by Doğan and Karakaş (2013) near Kozluca were most probably due to a simultaneous coseismic movement.

Elliott *et al.* (2013) was the first study to recognize the need for a second fault to explain the coseismic deformation by proposing a same-strike two-segment model (Fig. 12). While our main fault coincides with their western segment, their proposed eastern segment is not in agreement with the discontinuity that we observed in coseismic TSX range offsets south of Kozluca. It is clear that the morphology near Gedelova supports the existence of faulting as proposed by early field reports and then further discussed in their paper and later in the study of Mackenzie *et al.* (2016). However, our comparison tests using their published parameters show that the model with a tear fault fits better to our CSK coseismic interferogram, eliminating the necessity of a second subparallel fault segment to the east.

Another possible scenario could be a three-fault model that considers a complex rupture including the two parallel reverse-fault segments proposed by the studies of Elliott *et al.* (2013) and Wang *et al.* (2015), and the tear fault at Kozluca. Though plausible, we have not favored this scenario due to the discontinuity seen in the TSX range offsets. As discussed earlier, the geomorphology indeed has clear clues for an east–west-oriented thrust fault near Gedelova; however, it is unlikely for an active thrust segment here to cut through the structure seen in the TSX offsets. In addition, this complex scenario did not offer a better fit to our primary CSK dataset when compared to our two-fault model (Ⓔ Table S1; Ⓔ Figs. S4 and S5).

The existence of left-lateral tear faulting is also supported by the study of Işık *et al.* (2017) in which a clear cluster of aftershocks with strike-slip mechanisms is observed along a narrow zone that starts with the Kozluca fault to the south and continues to the north for ∼30 km toward the northeastern corner of Lake Van (Fig. 10d). The left-lateral character of the activity indicates that the Kozluca fault is probably a part of a tear/transform fault in the region. The possibility of a second segment is also supported by seismological studies. Similarly, Konca (2015) points out the difference in rupture velocity and/or rise time of the two slip patches that could be due to rupturing of the main fault and the tear fault. Based on postseismic GPS data, Dogan *et al.* (2014) also suggest that toward the east the earthquake rupture veers to the north running through Lake Erçek, supporting the presence of the tear fault we propose here.

Similar settings where thrust faulting during an earthquake is accompanied by strike-slip movements on adjacent tear faults (or lateral ramps) have been known since the 1971 San Fernando earthquake (Magistrale and Day, 1999). Other well-known examples of tear fault ruptures are the 1980 El Asnam, 1988 Spitak, 1994 Northridge, 2003 Zemmouri, 2005 Kashmir, and 2008 Wenchuan earthquakes (King and Yielding, 1984; Philip *et al.*, 1992; Belabbes *et al.*, 2009; Feng *et al.*, 2017). Tear faults either act as a barrier to impede the rupture or instead help it to jump to adjacent thrust segments. It is also possible that (like the Xiaoyudong fault in the Wenchuan case) the Kozluca fault could be a remnant part of an old strike-slip fault that was reactivated due to the rupture on the main Van fault. Further studies in the region might clarify the nature and extent of this newly recognized structure, which acted as a barrier in the case of the 2011 Van earthquake.

Fit to the near-field GPS stations is one area where our final model fails to improve on. As reported by Dogan *et al.* (2014) and Mackenzie *et al.* (2016), the area between the main Van fault and a splay fault to the south started deforming aseismically just after the earthquake. Using data from InSAR and a network of postseismic GPS stations, Dogan *et al.* (2014) proposed the existence of this splay and named it the Bostaniçi fault (Fig. 12). The near-field stations between the main Van fault and the Bostaniçi fault (i.e. VAAN and KAL2) could only be visited seven days after the event; as can be seen in Figure 3, they were clearly under the influence of this rapid postseismic motion. Whereas KALL continued to move northwards as in the coseismic period (Fig. 5), VAAN and KAL2 started moving southwestwards in the same manner as the newly occupied stations VN02, VN03 and VN04 which all reside on the hanging-wall of the main Van fault. Therefore, a discrepancy between our coseismic model and the GPS data is inevitable. We experimented with higher weights for the GPS dataset, but this did not significantly

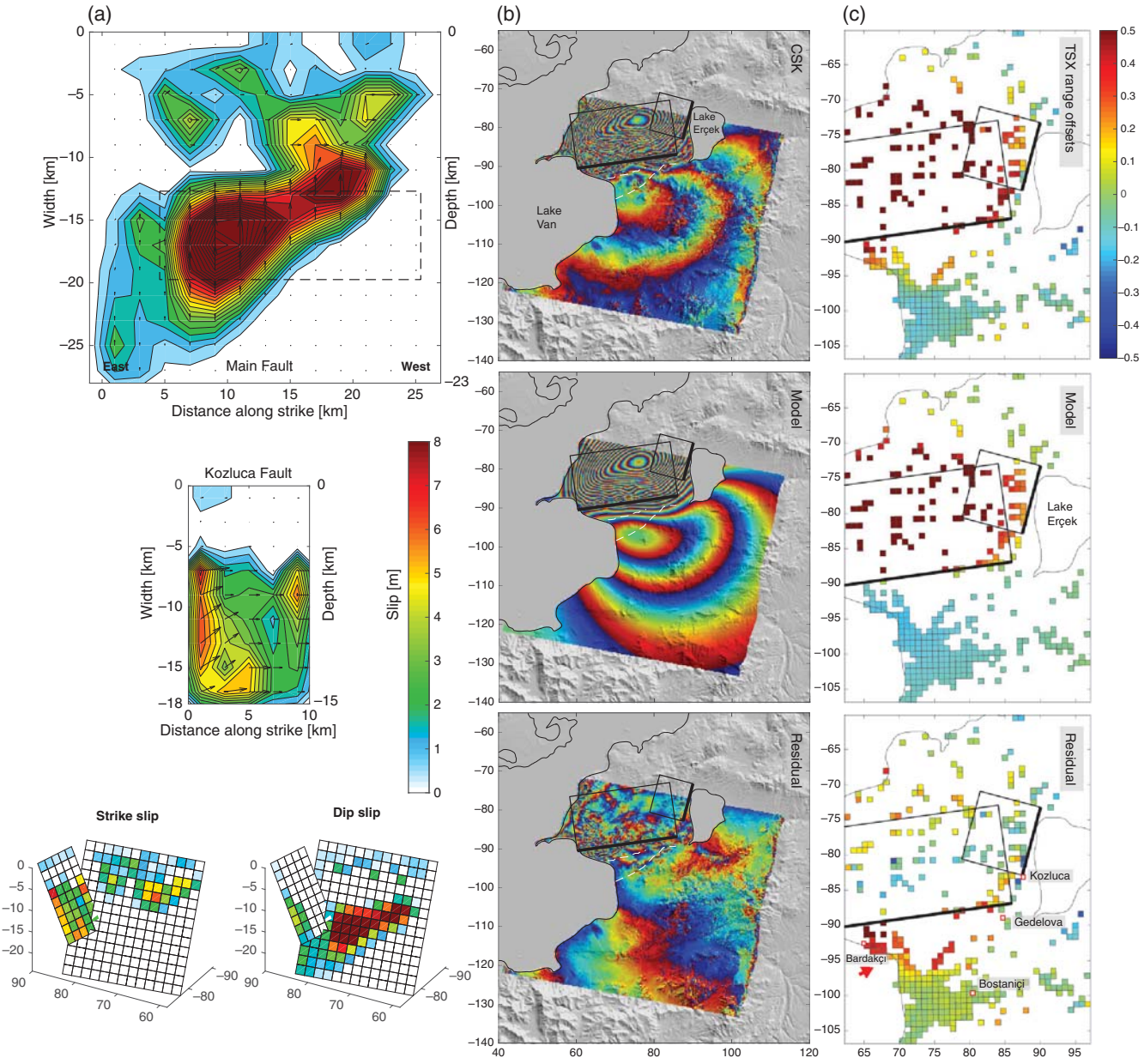

Figure 11. Modeling results for the two-segment model. (a) Slip distribution on the faults. The black dashed rectangle is the outline of the uniform-slip model for the main fault. (b) Data-model comparison of CSK-InSAR data (rewrapped to 5 cm). (c) Data-model comparison of TSX range offsets.

improve the fit. As in Dogan *et al.* (2014), an additional fault segment along the Bostaniçi fault is necessary to explain the motion recorded by the GPS data. Instead of discarding this dataset, we opted to use them by adopting significantly low weights in our modeling.

An early postseismic motion between Bardakçı and Bostaniçi is also evident in our coseismic InSAR data as well. The proposed Bostaniçi fault also coincides with the discontinuities observed in the coseismic CSK interferogram (Fig. 6c, black triangles). For the TSX data, the residuals shown with a red arrow to the south of our main fault in Figures 10c and 11c, in which positive values represent motion toward the satellite flying in an ascending orbit, suggest either an uplift or a left-lateral movement of this block. The southern boundary of these residuals coincides with the proposed Bostaniçi (Beyüzümü) fault. A later field study by Mackenzie *et al.* (2016) verified the postseismic movement along the western section of this discontinuity toward Lake Van. Both Dogan *et al.* (2014) and Mackenzie *et al.* (2016) agree on an overall model in which the Bostaniçi fault joins with the main Van fault to the north at depth. Judging by the distribution of the aftershocks in Figure 12, it is also possible that the 9 November 2011 M_w 5.7 event occurred on the offshore extension of the Bostaniçi fault. The eastern extent of

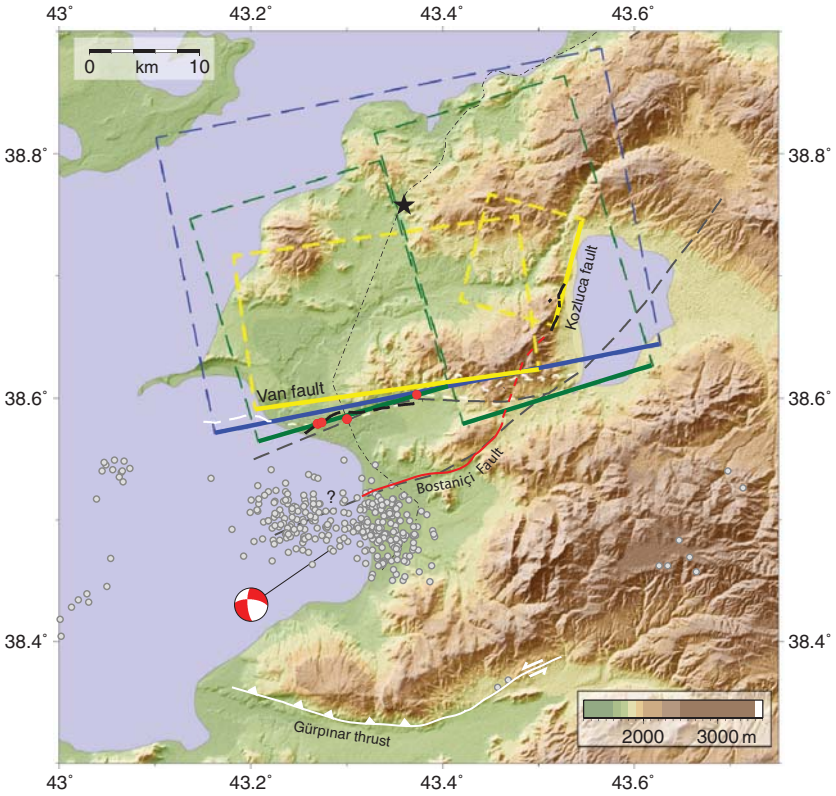

Figure 12. Overview of the study area showing the surface projection of our proposed Van and Kozluca faults (yellow dashed rectangles) with the previous single-fault model of Fielding *et al.* (2013) (blue dashed rectangle) and the two-segmented fault model of Elliott *et al.* (2013) (green dashed rectangles). Solid parts of these three rectangles represent the up-dip surface trace of the model faults. Similar to Figure 3, red dots are the locations where deformation of man-made structures was observed during the reconnaissance studies of Akyüz *et al.* (2011). Dashed gray lines show the proposed main faults from the study of Dogan *et al.* (2014) in the north and the proposed Bostaniçi fault in the south. The solid part of the red line representing the Bostaniçi fault is the same as Dogan *et al.* (2014), whereas we propose in this study that it possibly extends northeast toward the Kozluca fault (red dashed line). The Gürpınar thrust is modified from Selçuk (2016). The focal mechanism and the gray circles representing the aftershock activity near the 9 November 2011 M_w 5.7 event are from Işık *et al.* (2017).

this fault and its relationship with our proposed Kozluca fault in the east is also unknown. Since the Bostaniçi fault cuts through the Van city center, further geophysical and geological studies are crucial to study the fault at depth. The most recent earthquake activity in Van city before the 2011 event occurred in 1945, when buildings in the city center were reported to suffer heavy damage and collapses during the events that took place in the second half of that year (Lahn, 1946). Even though it is not clear, these events may have happened on a section of this splay fault or on the shallower parts of the main Van fault; therefore, a thorough study is essential to evaluate the seismic hazard to the city.

Like the splay to the south, the westernmost extent of the main Van fault rupture is also of importance. Recent underwater studies outlined by Özalp *et al.* (2016) propose that the main coseismic fault (Van fault) extends into Lake Van for about another 9 km. The closure pattern of the southernmost fringes of the CSK interferogram also hints of a possible extension of the fault into Lake Van. However, due to lack of deformation data to the west, we opt not to use a longer main fault to avoid slip artifacts.

While the occurrence of reverse and tear faulting is not surprising in a tectonic environment such as the Turkish–Iranian Plateau, its significance and role for the accommodation of the Arabian–Eurasian convergence has been a matter of debate (Copley and Jackson, 2006; Fielding *et al.*, 2013). When compared with the well-known strike-slip structures in the region, the seismic hazard associated with them is poorly understood. The 2011 Van earthquake indicates that, in addition to strike-slip faults, thrust faults in the region such as the Gürpınar thrust to the south of Van (Fig. 12) could also be playing a major role in the accommodation of the convergence. The Van event and the lack of corresponding clear surface ruptures have also increased the awareness of hazards due to blind-faulting events in the region.

Conclusions

In line with the earlier published studies on the 2011 Van earthquake, the results of our work using satellite geodetic observations show that the event was caused primarily by a rupture along a north-dipping blind-thrust fault. However, our model differs from earlier studies with the addition of a rupture along a tear fault to the west of Lake Erçek that pinpoints the eastern end of the rupture. Determining precisely where an earthquake rupture stops is an important parameter in seismic hazard analyses as high stress concentrations occur at the tip of the ruptures (King *et al.*, 1994).

To better delineate the fault structure beneath the surface, detailed geological and geophysical investigations in the future are necessary, leading to a better assessment of the seismic hazard around the city of Van. The splay fault that runs through the city center and its connection with the Kozluca fault should be studied in detail using a multidisciplinary approach.

Data and Resources

Most figures in this article were prepared using the Generic Mapping Tools (GMT) software package (Wessel and Smith, 1998). The Cosmo-SkyMed data are from the Italian Space Agency (ASI) projects 2142 and 2296; Envisat and

TerraSAR-X data are from the Group on Earth Observations (GEO) SuperSites project (http://supersites.earthobservations.org/van.php, last accessed February 2012).

Acknowledgments

The authors thank Martin Mai (King Abdullah University of Science and Technology [KAUST]), Yann Klinger (Institut de Physique du Globe de Paris [IPG Paris]), Robert Reilinger (Massachusetts Institute of Technology [MIT]), Mustapha Meghraoui (Ecole et Observatoire des Sciences de la Terre [EOST], University of Strasbourg), Hannes Vasyura-Bathke (KAUST), Serdar Kalkavan (Devlet Su İşleri-General Directorate of State Hydraulic Works [DSİ] Ankara), and many others for sharing their insights. The authors also thank Diego Melgar and an anonymous reviewer for their constructive comments on the article. A high-resolution digital elevation model (DEM) of the epicentral area is generously provided by Korhan Erturaç (Sakarya University [SAÜ]). The research reported in this publication was supported by KAUST.

References

Aksoy, E., and Y. Tatar (1990). Van ili Doğu–Kuzeydoğu yöresinin stratigrafisi ve tektoniği, *Doğa Turkish J. Eng. Environ. Sci.* **14,** 628–644 (in Turkish).

Akyüz, S., C. Zabcı, and T. Sancar (2011). Preliminary report on the 23 October 2011 Van earthquake, *Technical Report*, İstanbul Teknik Üniversitesi.

Belabbes, S., C. Wicks, Z. Cakir, and M. Meghraoui (2009). Rupture parameters of the 2003 Zemmouri (M_w 6.8), Algeria, earthquake from joint inversion of interferometric synthetic aperture radar, coastal uplift, and GPS, *J. Geophys. Res.* **114,** no. B3, doi: 10.1029/2008JB005912.

Berberian, M. (2014). *Earthquakes and Coseismic Surface Faulting on the Iranian Plateau*, Elsevier Science, Amsterdam, The Netherlands.

Bevere, L., R. Enz, J. Mehlhorn, and T. Tomura (2012). *Natural Catastrophes and Man-Made Disasters in 2011: Historic Losses Surface from Record Earthquakes and Floods*, Sigma 2, SwissRe, Zurich, Switzerland.

Bro, R., and S. De Jong (1997). A fast non-negativity-constrained least squares algorithm, *J. Chemometrics* **11,** 392–401.

Calais, E., A. Freed, G. Mattioli, F. Amelung, S. Jónsson, P. Jansma, S. H. Hong, T. Dixon, C. Prépetit, and R. Momplaisir (2010). Transpressional rupture of an unmapped fault during the 2010 Haiti earthquake, *Nature Geosci.* **3,** no. 11, 794–799.

Copley, A., and J. Jackson (2006). Active tectonics of the Turkish-Iranian plateau, *Tectonics* **25,** no. 6, doi: 10.1029/2005TC001906.

Dewey, J. F., M. R. Hempton, W. S. F. Kidd, F. T. Saroglu, and A. M. C. Şengör (1986). Shortening of continental lithosphere: The neotectonics of Eastern Anatolia—A young collision zone, *Geol. Soc. Lond. Spec. Publ.* **19,** no. 1, 1–36.

Dhont, D., and J. Chorowicz (2006). Review of the neotectonics of the Eastern Turkish-Armenian plateau from geomorphic analysis of digital elevation model imagery, *Int. J. Earth Sci.* **95,** 34–49, doi: 10.1007/s00531-005-0020-3.

Doğan, B., and A. Karakaş (2013). Geometry of co-seismic surface ruptures and tectonic meaning of the 23 October 2011 M_w 7.1 Van earthquake (East Anatolian Region, Turkey), *J. Struct. Geol.* **46,** 99–114.

Dogan, U., D. Ö. Demir, Z. Çakir, S. Ergintav, H. Ozener, A. M. Akoğlu, S. S. Nalbant, and R. Reilinger (2014). Postseismic deformation following the M_w 7.2, 23 October 2011 Van earthquake (Turkey): Evidence for aseismic fault reactivation, *Geophys. Res. Lett.* **41,** no. 7, 2334–2341.

Dolan, J. F., S. A. Christofferson, and J. H. Shaw (2003). Recognition of paleoearthquakes on the Puente Hills blind thrust fault, California, *Science* **300,** no. 5616, 115–118.

Ekström, G., M. Nettles, and A. M. Dziewonski (2012). The Global CMT project 2004–2010: Centroid-moment tensors for 13,017 earthquakes, *Phys. Earth Planet. In.* **200/201,** 1–9, doi: 10.1016/j.pepi.2012.04.002.

Elliott, J. R., A. C. Copley, R. Holley, K. Scharer, and B. Parsons (2013). The 2011 M_w 7.1 Van (eastern Turkey) earthquake, *J. Geophys. Res.* **118,** no. 4, 1619–1637.

Emre, Ö., T. Duman, S. Özalp, and H. Elmacı (2011). 23 Ekim 2011 Van Depremi Saha Gözlemleri ve Kaynak Faya İlişkin Ön Değerlendirmeler, *Technical Report*, General Directorate of Mineral Research and Exploration, Ankara, Turkey (in Turkish).

Erdik, M., Y. Kamer, M. Demircioğlu, and K. Şeşetyan (2012). 23 October 2011 Van (Turkey) earthquake, *Nat. Hazards* **64,** no. 1, 651–665.

Feng, G., S. Jónsson, and Y. Klinger (2017). Which fault segments ruptured in the 2008 Wenchuan earthquake and which did not? New evidence from near-fault 3D surface displacements derived from SAR image offsets, *Bull. Seismol. Soc. Am.* **107,** no. 3, 1185–1200.

Feng, W., Z. Li, T. Hoey, Y. Zhang, R. Wang, S. Samsonov, Y. Li, and Z. Xu (2014). Patterns and mechanisms of coseismic and postseismic slips of the 2011 M_w 7.1 Van (Turkey) earthquake revealed by multi-platform synthetic aperture radar interferometry, *Tectonophysics* doi: 10.1016/j.tecto.2014.06.011.

Fielding, E. J., P. R. Lundgren, T. Taymaz, S. Yolsal-Çevikbilen, and S. E. Owen (2013). Fault-slip source models for the 2011 M 7.1 Van earthquake in Turkey from SAR interferometry, pixel offset tracking, GPS, and seismic waveform analysis, *Seismol. Res. Lett.* **84,** no. 4, 579–593.

Hayes, G. P., R. W. Briggs, A. Sladen, E. J. Fielding, C. Prentice, K. Hudnut, P. Mann, F. W. Taylor, A. J. Crone, R. Gold, *et al.* (2010). Complex rupture during the 12 January 2010 Haiti earthquake, *Nature Geosci.* **3,** no. 11, 800–805.

Irmak, T. S., B. Doğan, and A. Karakaş (2012). Source mechanism of the 23 October, 2011, Van (Turkey) earthquake ($M_w = 7.1$) and aftershocks with its tectonic implications, *Earth Planets Space* **64,** 991–1103, doi: 10.5047/eps.2012.05.002.

Işık, S. E., A. Ö. Konca, and H. Karabulut (2017). The seismic interactions and spatiotemporal evolution of seismicity following the October 23, 2011 M_w 7.1 Van, eastern Anatolia earthquake, *Tectonophysics* **702,** 8–18, doi: 10.1016/j.tecto.2017.02.024.

Jónsson, S., H. A. Zebker, P. Segall, and F. Amelung (2002). Fault slip distribution of the 1999 M_w 7.2 Hector Mine earthquake, California, estimated from satellite radar and GPS measurements, *Bull. Seismol. Soc. Am.* **92,** no. 4, 1377–1389.

Karimzadeh, S., Z. Cakir, B. Osmanoğlu, G. Schmalzle, M. Miyajima, R. Amiraslanzadeh, and Y. Djamour (2013). Interseismic strain accumulation across the North Tabriz Fault (NW Iran) deduced from InSAR time series, *J. Geodyn.* **66,** 53–58.

Ketin, İ. (1977). Van Gölü ile İran sınırı arasındaki bölgede yapılan jeoloji gözlemlerinin sonuçları hakkında kısa bir açıklama, *Türkiye Jeoloji Kurumu Bülteni* **20,** 79–85 (in Turkish).

King, G., and G. Yielding (1984). The evolution of a thrust fault system: Processes of rupture initiation, propagation and termination in the 1980 El Asnam (Algeria) earthquake, *Geophys. J. Int.* **77,** no. 3, 915–933.

King, G. C., R. S. Stein, and J. Lin (1994). Static stress changes and the triggering of earthquakes, *Bull. Seismol. Soc. Am.* **84,** no. 3, 935–953.

King, G. C. P., and C. Vita-Finzi (1981). Active folding in the Algerian earthquake of 10 October 1980, *Nature* **292,** no. 5818, 22–26, doi: 10.1038/292022a0.

Koçyiğit, A., A. Yilmaz, S. Adamia, and S. Kuloshvili (2001). Neotectonics of east Anatolian Plateau (Turkey) and lesser Caucasus: Implications for transition from thrusting to strike-slip faulting, *Geodin. Acta* **14,** 177–195.

Konca, A. O. (2015). Rupture process of 2011 M_w 7.1 Van, eastern Turkey earthquake from joint inversion of strong-motion, high-rate GPS, teleseismic, and GPS data, *J. Seismol.* **19,** no. 4, 969–988.

Lahn, E. (1946). Van mıntıkası yer sarsıntıları hakkında not, *Maden Tetkik ve Arama Dergisi* **35,** 126–132 (in Turkish).

Mackenzie, D., J. R. Elliott, E. Altunel, R. T. Walker, Y. C. Kurban, J.-L. Schwenninger, and B. Parsons (2016). Seismotectonics and rupture process of the M_w 7.1 2011 Van reverse-faulting earthquake, eastern Turkey, and implications for hazard in regions of distributed

shortening, *Geophys. J. Int.* **206,** no. 1, 501–524, doi: 10.1093/gji/ggw158.

Magistrale, H., and S. Day (1999). 3D simulations of multi-segment thrust fault rupture, *Geophys. Res. Lett.* **26,** no. 14, 2093–2096.

McClusky, S., S. Balassanian, A. Barka, C. Demir, S. Ergintav, I. Georgiev, O. Gurkan, M. Hamburger, K. Hurst, H. Kahle, *et al.* (2000). Global Positioning System constraints on plate kinematics and dynamics in the eastern Mediterranean and Caucasus, *J. Geophys. Res.* **105,** no. B3, 5695–5719.

Meghraoui, M., S. Maouche, B. Chemaa, Z. Cakir, A. Aoudia, A. Harbi, P.-J. Alasset, A. Ayadi, Y. Bouhadad, and F. Benhamouda (2004). Coastal uplift and thrust faulting associated with the $M_w = 6.8$ Zemmouri (Algeria) earthquake of 21 May, 2003, *Geophys. Res. Lett.* **31,** no. L19605, doi: 10.1029/2004GL020466.

Miranda, N., B. Duesmann, M. Pinol, D. Giudici, and D. D'Aria (2010). Impact of Envisat mission extension on SAR data, *Technical Note*, ESA, 12 October 2010.

Moro, M., V. Cannelli, M. Chini, C. Bignami, D. Melini, S. Stramondo, M. Saroli, M. Picchiani, C. Kyriakopoulos, and C. A. Brunori (2014). The October 23, 2011, Van (Turkey) earthquake and its relationship with neighbouring structures, *Sci. Rept.* **4,** 3959, doi: 10.1038/srep03959.

Okada, Y. (1985). Surface deformation due to shear and tensile faults in a half-space, *Bull. Seismol. Soc. Am.* **75,** no. 4, 1135–1154.

Örgülü, G., M. Aktar, N. Türkelli, E. Sandvol, and M. Barazangi (2003). Contribution to the seismotectonics of Eastern Turkey from moderate and small size events, *Geophys. Res. Lett.* **30,** no. 24, 8040.

Ortlieb, L., S. Barrientos, and N. Guzman (1996). Coseismic coastal uplift and coralline algae record in northern Chile: The 1995 Antofagasta earthquake case, *Quaternary Sci. Rev.* **15,** nos. 8/9, 949–960.

Özalp, S., B. S. Aydemir, Ş. Olgun, B. Şimşek, H. Elmacı, M. Evren, Ö. Emre, M. B. Aydın, O. Kurtuluş, F. Öcal, *et al.* (2016). Van Gölü (Edremit Körfezi) Kuvaterner Çökellerinde Tektonik Deformasyonlar, Doğu Anadolu, Türkiye, *Maden Tetkik ve Arama Dergisi* **153,** 45–62, doi: 10.19076/mta.65720 (in Turkish).

Özkaymak, Ç. (2003). Van Şehri Yakın Çevresinin Aktif Tektonik Özellikleri, *M.Sc. Thesis*, Yüzüncü Yıl University, Faculty of Sciences, Van, Turkey, 76 (in Turkish).

Parsons, B., T. Wright, P. Rowe, J. Andrews, J. Jackson, R. Walker, M. Khatib, M. Talebian, E. Bergman, and E. R. Engdahl (2006). The 1994 Sefidabeh (eastern Iran) earthquakes revisited: New evidence from satellite radar interferometry and carbonate dating about the growth of an active fold above a blind thrust fault, *Geophys. J. Int.* **164,** no. 1, 202–217.

Philip, H., and M. Meghraoui (1983). Structural analysis and interpretation of the surface deformations of the El Asnam earthquake of October 10, 1980, *Tectonics* **2,** no. 1, 17–49, doi: 10.1029/TC002i001p00017.

Philip, H., E. Rogozhin, A. Cisternas, J. C. Bousquet, B. Borisov, and A. Karakhanian. (1992). The Armenian earthquake of 1988 December 7: Faulting and folding, neotectonics and palaeoseismicity, *Geophys. J. Int.* **110,** no. 1, 141–158.

Pınar, A., Y. Honkura, K. Kuge, M. Matsushima, N. Sezgin, M. Yılmazer, and Z. Öğütçü (2007). Source mechanism of the 2000 November 15 Lake Van earthquake ($M_w = 5.6$) in eastern Turkey and its seismotectonic implications, *Geophys. J. Int.* **170,** no. 2, 749–763.

Reilinger, R. E., S. McClusky, P. Vernant, S. Lawrence, S. Ergintav, R. Cakmak, H. Ozener, F. Kadirov, I. Guliev, R. Stepanyan, *et al.* (2006). GPS constraints on continental deformation in the Africa-Arabia-Eurasia continental collision zone and implications for the dynamics of plate interactions, *J. Geophys. Res.* **111,** V05411, doi: 10.1029/2005JB004051.

Rosen, P. A., S. Hensley, G. Peltzer, and M. Simons (2004). Updated repeat orbit interferometry package released, *Eos Trans. AGU* **85,** 47.

Şaroğlu, F., Ö. Emre, and İ. Kuşçu (1992). *Active Fault Map of Turkey*, General Directorate of Mineral Research and Exploration (MTA), Ankara, Turkey.

Selçuk, A. S. (2016). Evaluation of the relative tectonic activity in the eastern Lake Van basin, East Turkey, *Geomorphology* **270,** 9–21.

Selçuk, A. S., M. K. Erturaç, and S. Nomade (2016). Geology of the Çaldıran fault, eastern Turkey: Age, slip rate and implications on the characteristic slip behaviour, *Tectonophysics* **680,** 155–173.

Şengör, A. M. C., N. Görür, and F. Şaroğlu (1985). Strike-slip faulting and related basin formation in zones of tectonic escape: Turkey as a case study, in *Strike-Slip Deformation, Basin Formation, and Sedimentation*, K. T. Biddle and N. Christie-Blick (Editors), Vol. 37, Society of Economic Paleontologists and Mineralogists Special Publication, Tulsa, Oklahoma, 227–264 (in honor of J. C. Crowell).

Sudhaus, H., and S. Jónsson (2009). Improved source modelling through combined use of InSAR and GPS under consideration of correlated data errors: Application to the June 2000 Kleifarvatn earthquake, Iceland, *Geophys. J. Int.* **176,** 389–404, doi: 10.1111/j.1365-246X.2008.03989.x.

Sudhaus, H., and S. Jónsson (2011). Source model for the 1997 Zirkuh earthquake ($M_w = 7.2$) in Iran derived from JERS and ERS InSAR observations, *Geophys. J. Int.* **185,** 676–692.

Tan, O. (2004). Kafkasya, Doğu Anadolu ve Kuzeybatı İran Depremlerinin Kaynak Mekanizması Özellikleri ve Yırtılma Süreçleri, *Ph.D. Thesis*, İstanbul Teknik Üniversitesi, İstanbul (in Turkish).

Toksöz, M. N., E. Arpat, and F. Şaroğlu (1977). East Anatolia earthquake of 24 November, 1976, *Nature* **270,** 423–425.

Trasatti, E., C. Tolomei, G. Pezzo, S. Atzori, and S. Salvi (2016). Deformation and related slip due to the 2011 Van earthquake (Turkey) sequence imaged by SAR data and numerical modeling, *Rem. Sens.* **8,** no. 6, 532.

Türkelli, N., E. Sandvol, E. Zor, R. Gok, T. Bekler, A. Al-Lazki, H. Karabulut, S. Kuleli, T. Eken, C. Gurbuz, *et al.* (2003). Seismogenic zones in eastern Turkey, *Geophys. Res. Lett.* **30,** no. 24, doi: 10.1029/2003GL018023.

Wang, C., X. Ding, Q. Li, X. Shan, W. Zhu, B. Guo, and P. Liu (2015). Coseismic and postseismic slip models of the 2011 Van earthquake, Turkey, from InSAR, offset-tracking, MAI, and GPS observations, *J. Geodyn.* **91,** 39–50, doi: 10.1016/j.jog.2015.08.006.

Wang, T., and S. Jónsson (2015). Improved SAR amplitude image offset measurements for deriving three-dimensional coseismic displacements, *IEEE J. Sel. Topics Appl. Earth Observ. Remote Sens.* doi: 10.1109/JSTARS.2014.2387865.

Werner, C. L., U. Wegmüller, T. Strozzi, and A. Wiesmann (2000). Gamma SAR and interferometric processing software, *Proc. of the ERS-Envisat Symposium*, Gothenburg, Sweden, 16–20 October 2000.

Wessel, P., and W. H. F. Smith (1998). New, improved version of Generic Mapping Tools released, *Eos Trans. AGU* **79,** no. 47, 579, doi: 10.1029/98EO00426.

Wright, T., E. Fielding, and B. Parsons (2001). Triggered slip: Observations of the 17 August 1999 Izmit (Turkey) earthquake using radar interferometry, *Geophys. Res. Lett.* **28,** no. 6, 1079–1082.

Zor, E., E. Sandvol, C. Gürbüz, N. Türkelli, D. Seber, and M. Barazangi (2003). The crustal structure of the East Anatolian plateau from receiver functions, *Geophys. Res. Lett.* **30,** no. 24, 8044.

King Abdullah University of Science and Technology (KAUST)
Thuwal 23955, Saudi Arabia
akoglua@itu.edu.tr
sigurjon.jonsson@kaust.edu.sa
(A.M.A., S.J.)

Earth Observatory of Singapore (EOS)
Nanyang Technological University
50 Nanyang Avenue, Block N2-01a-15
Singapore 639798
Republic of Singapore
wang.teng@ntu.edu.sg
(T.W.)

Department of Geology
Faculty of Mines
Istanbul Technical University
Ayazağa Yerleşkesi
Sarıyer 34469
Istanbul, Turkey
ziyadin.cakir@itu.edu.tr
zabci@itu.edu.tr
(Z.Ç., C.Z.)

Department of Geomatics
Yıldız Technical University
Davutpaşa Yerleşkesi
Esenler 34220
Istanbul, Turkey
dogan@yildiz.edu.tr
alpayoz@yildiz.edu.tr
(U.D., A.Ö.)

Department of Geodesy
Kandilli Observatory and Earthquake Research Institute
Boğaziçi University
Çengelköy 34684
Istanbul, Turkey
semih.ergintav@boun.edu.tr
(S.E.)

NASA Goddard Space Flight Center
Greenbelt, Maryland 20771
batuhan.osmanoglu@nasa.gov
(B.O.)

School of Geosciences and Info-Physics
Central South University
Changsha 410083
China
fredgps@csu.edu.cn
(G.F.)

Fugro Sial Ltd.
Farabi Sokak 40/4
06680 Ankara, Turkey
o.emre@fugro.com
(Ö.E.)

Manuscript received 18 October 2017;
Published Online 3 July 2018